

Experimental test of models of high-plasma-density, radio-frequency sheaths

Mark A. Sobolewski

National Institute of Standards and Technology, Gaithersburg, Maryland 20899-8362

(Received 22 July 1998)

Measurements of the rf-bias current and voltage applied to the substrate electrode of a high-density plasma reactor, combined with dc measurements of the ion current at the electrode and capacitive probe measurements of the plasma potential, enabled a rigorous, quantitative test of models of the electrical properties of the sheath adjacent to the electrode. The measurements were performed for argon discharges at 1.33 Pa (10 mTorr), ion current densities of 1.3–13 mA/cm², rf-bias frequencies of 0.1–10 MHz, and rf-bias voltages from less than 1 to more than 100 V. From the measurements, the current, voltage, impedance, and power of the sheath adjacent to the electrode were determined and were compared to model predictions. The properties of the opposing sheath, adjacent to grounded surfaces, were also determined. The behavior of the two sheaths ranged from nearly symmetric to very asymmetric. Changes in the symmetry are explained by models of the sheath impedance. [S1063-651X(99)03501-1]

PACS number(s): 52.40.Hf, 52.70.Gw, 52.70.Ds

I. INTRODUCTION

In capacitively coupled, low-density plasma reactors, electrical discharges are generated by passing radio-frequency (rf) current between two electrodes. The rf current flows through the space-charge sheath adjacent to each electrode, resulting in a radio-frequency modulation in the sheath voltage and sheath width. Such rf modulated sheaths have important, nonlinear electrical properties that are not completely understood. Usually, rf sheaths make dominant contributions to the electrical properties of the discharge and they play an important role in the mechanisms by which the rf power is absorbed [1–3]. Models of the impedance of rf sheaths can be used to predict ion bombardment energies [4–10]. Models of the nonlinear electrical properties of rf sheaths predict how the plasma is affected by the circuitry that surrounds it [11,12]. Sheath models can also be used to interpret electrical measurements, allowing these measurements to monitor changes in ion energies [13,14], ion current [15–17], or plasma density [18].

In high-density plasma reactors, plasmas are generated by inductive sources [19], electron cyclotron resonance sources [20], helical resonators [21], or helicon sources [22], but the substrate electrode is also usually powered by a separate, capacitively coupled “rf-bias” power supply, to control the kinetic energy of ions bombarding the substrate. The interaction of the rf-bias power with the plasma depends strongly on sheath properties. Models of the electrical properties of the sheaths in high-density plasmas are needed to predict sheath voltages, ion energies and etch rates [23–26], and to develop new types of electrical sensors for monitoring high-density plasmas [27,28].

Many models of the electrical properties of rf plasma sheaths have been proposed, covering a variety of different regimes of frequency and pressure. First, at frequencies $\omega \ll \omega_i$, where ω_i is the ion plasma frequency, there is a low-frequency regime where ions are in equilibrium with the rf field and only conduction current need be considered—the displacement current is negligible [7,8,29,30]. Second, there is a high-frequency regime, $\omega \gg \omega_i$, where ions only follow the time-averaged field, and the displacement current domi-

nates the conduction current [29,31–39]. Finally, there is an intermediate region, where ions are wholly or partly able to follow the rf fields, and the conduction current and the displacement current are comparable [12,40–44]. Some models cover the low-pressure regime, in which collisions of ions in the sheath can be neglected [7,8,12,31,33,34,40,42–44]; other models, designed for higher pressures, include ion collisions [29,30,32,33,35–39,41]. Low-density plasma reactors are often operated in the high-frequency, high-pressure regime. High-density plasma reactors are typically operated with higher ω_i , thinner sheaths, and lower pressures, so high-density sheaths are believed to fall instead in the low-pressure regime and the low- or intermediate-frequency regime.

Despite this abundance of modeling work, experimental tests of sheath models are only rarely reported. Many experimental studies of the current-voltage characteristics of rf discharges have been performed, but these studies usually do not provide enough information to rigorously test the models. Usually, only a single voltage is measured, the voltage on the powered electrode, which is the sum of the voltage drops across two opposing sheaths. To test sheath models, however, the individual sheath voltages need to be determined. This can be accomplished if one also measures the rf voltage on a wire probe inserted into the plasma [2,45]. Measurements of the total ion current at a powered electrode [46] provide additional information. In a previous study in a low-density reactor, wire probe and ion current measurements, combined with measurements of the rf current and voltage at the powered electrode, enabled a rigorous test of rf sheath models [39,47]. In this paper, the same methods are applied to test models under very different conditions in a high-density reactor. The measurements provide a complete, quantitative test for the sheath at the rf-biased electrode. They also provide a detailed analysis of the opposing sheath at grounded surfaces. The two sheaths behave rather symmetrically at low rf-bias frequencies, but less symmetrically at higher frequencies. The asymmetry at high frequencies, which strongly affects the kinetic energy of ions bombarding reactor surfaces, is explained by sheath models.

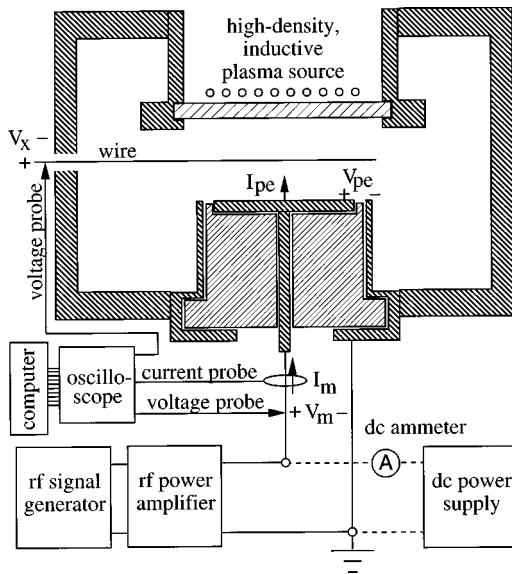


FIG. 1. Diagram of the discharge cell showing the polarity of the current $I_m(t)$ and voltage $V_m(t)$ measured on the rf-bias feed to the lower electrode, the current $I_{pe}(t)$ and the voltage $V_{pe}(t)$ at the electrode, and the voltage $V_x(t)$ measured on a wire inserted into the plasma.

II. EXPERIMENT

Experiments were performed in a Gaseous Electronics Conference (GEC) reference cell [48] (Fig. 1), in which the standard upper electrode was replaced by an inductive, high-density plasma source. The source [49] consisted of a five-turn, planar coil, grounded at one end and powered at the other end at 13.56 MHz. An electrostatic shield [50] was placed below the coil, insulated from it by a quartz disk. Another quartz disk beneath the shield was sealed to the vacuum chamber. Gas (argon at 5 sccm) flowed into the cell through a 2.75 inch side port. The gas outlet was a 6 inch port on which a turbo pump was mounted. Pressure in the cell was controlled at 1.33 Pa (10 mTorr) by varying the rotation speed of the turbo.

The standard, lower electrode assembly consisted of a 10.2-cm-diam aluminum electrode and a stainless steel ground shield, separated by an alumina insulator. In previous studies [49,50], a steel plate of diameter 16.5 cm was placed on the lower electrode to increase its effective area. The steel plate, however, may introduce edge effects and back-side effects that would make the electrical analysis of the electrode and its sheath more complicated. Therefore, in this study the steel plate was removed.

The lower electrode was powered at variable frequencies (100 kHz, 1.00 MHz, and 10.17 MHz) using a signal generator and a power amplifier (Amplifier Research 150A100) [51]. Capacitors inside the amplifier acted as blocking capacitors, allowing a dc self-bias voltage to be generated on the lower electrode. No external blocking capacitors were used. Also, no matching network was used, because satisfactory power delivery was obtained without one. Power was applied to the electrode for only a few seconds for each experimental condition, to minimize sputtering of aluminum from the electrode surface.

A Pearson model 2877 current probe [51] and a LeCroy model PP002 voltage probe [51] were mounted on the lead

that powers the lower electrode. Another PP002 voltage probe was attached to a wire probe [2] inserted into the plasma. Signals acquired by the probes were digitized by a LeCroy 9354A oscilloscope [51] capable of real-time sampling at a rate of $5 \times 10^8 \text{ s}^{-1}$. Digitized wave forms were transferred to a computer, which used a curve fitting algorithm [52] to determine the magnitude and phase of their Fourier components at the rf-bias frequency, at the inductive source frequency, and at harmonic frequencies, as well as their dc components. Using techniques described previously [53], phase errors caused by propagation delays in the lines connecting the probes to the oscilloscope were measured and accounted for, within an error of $\pm 1^\circ$. Magnitude errors were estimated by comparing probe amplitudes to amplitudes measured directly by the oscilloscope. Below 20 MHz, excellent agreement was obtained. In that range, the accuracy of the measurements is mostly limited by the oscilloscope, which is estimated to be $\pm 3\%$. Above 30 MHz, however, the accuracy of the probes degrades rapidly.

III. RESULTS

A. Current and voltage at the rf-bias electrode

The current $I_{pe}(t)$ flowing from the surface of the powered electrode into the plasma, and the voltage $V_{pe}(t)$ between the powered electrode and its ground shield, differ from $I_m(t)$ and $V_m(t)$, the current and voltage measured some distance away (Fig. 1), because of parasitic stray impedances located between the measurement point and the electrode. Using techniques described previously [2,53], these parasitics were characterized, allowing us to determine $I_{pe}(t)$ and $V_{pe}(t)$ from $I_m(t)$ and $V_m(t)$. Values for the parasitics are similar to values previously reported from the original, low-density GEC cells [2,48,53].

Figure 2 shows $I_{pe}(t)$ and $V_{pe}(t)$ wave forms measured as a function of rf-bias power. At zero rf bias, one only observes rf components at the driving frequency of the inductive source (13.56 MHz) and at its harmonics. The inductive source injects rf current into the plasma, and some of this current flows to the electrode, contributing to $I_{pe}(t)$. From there, the current flows through the rf-bias circuitry or through cell parasitics to ground, generating an rf voltage that contributes to $V_{pe}(t)$. Due to blocking capacitors, the electrode draws no dc current from the plasma. Therefore, the electrode “floats” at a small, positive dc voltage V_{pef} , visible in Fig. 2 and given in Table I, at which the time-averaged electron and ion currents to the electrode are equal.

When rf bias is applied, one observes voltage and current components at the rf-bias frequency and its harmonics, as well as the inductive source frequency and its harmonics. At low rf-bias voltages, $I_{pe}(t)$ resembles a sinusoid. As the rf-bias amplitude increases, $I_{pe}(t)$ becomes less sinusoidal and the dc component of $V_{pe}(t)$, V_{pe0} , becomes increasingly negative, because of nonlinear properties of the sheaths to be discussed below. At high rf-bias amplitudes, $V_{pe}(t)$ also becomes nonsinusoidal. Although the voltage generated by the amplifier, $V_a(t)$, is presumably sinusoidal, $V_{pe}(t)$ differs from $V_a(t)$, according to

$$V_a(t) = V_{pe}(t) + I_{pe}(t)R_a, \quad (1)$$

where R_a is the 50- Ω series output resistance of the rf amplifier.

TABLE I. Electrical properties measured with no rf bias applied, as a function of inductive source power (P_L), including the dc voltages on the powered electrode (V_{pef}), on the wire probe (V_{xf}), at the center of the plasma (V_{bf} , obtained from measurements in Refs. [49,50]), from the center of the plasma to the powered electrode (V_{psf}), and across the sheath surrounding the wire probe (V_{bxf}); and the ion current (I_0) and ion current density (J_0) at the powered electrode.

P_L (W)	V_{pef} (V)	V_{xf} (V)	V_{bf} (V)	$-V_{psf}$ (V)	V_{bxf} (V)	I_0 (A)	J_0 (mA/cm ²)
60	7.0	6.4	21.0	14.0	14.6	0.105	1.3
120	6.2	5.5	21.0	14.8	15.5	0.320	4.0
350	5.9	4.7	21.0	15.1	16.3	1.05	13.0

B. Plasma potential

To determine the time-dependent potential in the plasma, a wire probe [2] was inserted into the plasma. As shown in Fig. 1, a voltage probe was mounted on the wire, outside vacuum, to measure $V_x(t)$, the voltage difference between the wire and the flange on which it was mounted. The potential in the plasma surrounding the wire, $V_b(t)$, is given by

$$V_b(t) = V_x(t) + V_{bx}(t), \quad (2)$$

where $V_{bx}(t)$ is the voltage drop across the sheath that separates the wire from the plasma. Procedures have been developed [45] to determine the rf components of $V_{bx}(t)$ and $V_b(t)$ from $V_x(t)$ measurements. Using these procedures, an initial survey was performed, which showed that, as long as the source was operated in the bright, high-density, inductive mode, rf components of $V_{bx}(t)$ were always ≤ 0.1 V, small enough to be neglected in all subsequent measurements. These components are smaller than those measured previously in lower-density plasmas [2] because the width and impedance of the wire sheath are smaller at higher plasma density.

In contrast, the dc component of $V_{bx}(t)$ cannot be neglected. The dc components of $V_{bx}(t)$, $V_x(t)$, and $V_b(t)$, when no rf bias is applied, are denoted V_{bxf} , V_{xf} , and V_{bf} . Wire probe measurements of V_{xf} ranged from 4.7 to 6.4 V, but Langmuir probe measurements [49,50] indicate that V_{bf} is 21 V (see Table I). Thus

$$V_{bxf} = V_{bf} - V_{xf}, \quad (3)$$

is 15–16 V, certainly not negligible. The dc voltage V_{bxf} acts to repel plasma electrons from the wire probe, thus maintaining a balance between the flow of electrons and ions from the plasma to the wire. These currents must balance; because the wire probe has a high dc impedance to ground (1 M Ω) it draws negligible dc current from the plasma. To repel enough electrons to satisfy the zero net current condition, V_{bxf} must be several times the mean kinetic energy of electrons in the vicinity of the wire.

When rf bias is applied, the dc plasma potential and the dc voltage on the wire probe may change, but the difference between them will not change (unless the rf bias perturbs the local electron energies in the vicinity of the wire probe). Thus, the plasma potential $V_b(t)$ can be determined from

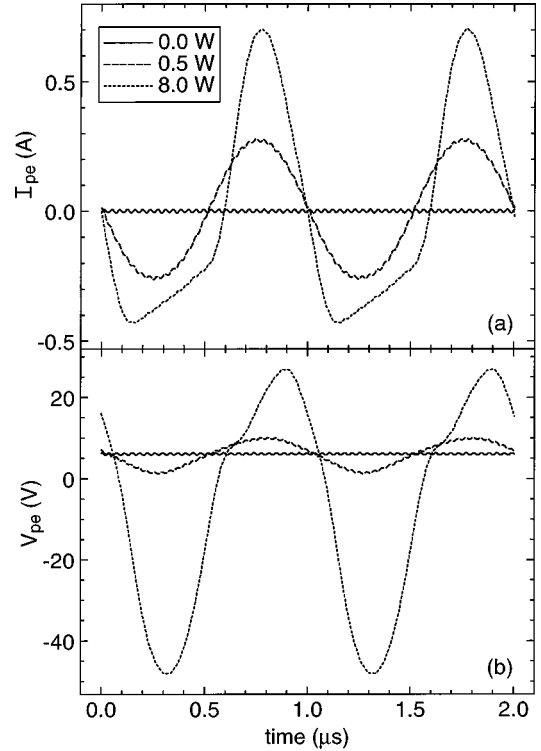


FIG. 2. Wave forms of (a) current at the powered electrode, $I_{pe}(t)$, and (b) voltage between the powered electrode and its ground shield, $V_{pe}(t)$, at an inductive source power of 120 W and rf-bias powers (P_{pe}) of 0.0, 0.5, and 8.0 W. The rf-bias frequency is 1 MHz.

$$V_b(t) = V_x(t) + V_{bxf}. \quad (4)$$

It should be noted that $V_b(t)$, like the $V_x(t)$ waveform from which it is derived, is referenced to the middle of the chamber wall.

Figure 3 shows $V_b(t)$ wave forms as a function of rf-bias power. At zero rf bias, in Fig. 3(a), rf components are only observed at the inductive source frequency and its harmonics. These components are small, ~ 1 V, as noted previously [49]. For low rf-bias amplitudes, as in Fig. 3(b), $V_b(t)$ resembles a sinusoid at the rf-bias frequency added to the higher-frequency oscillation produced by the inductive source. At higher rf-bias amplitudes, as in Fig. 3(c), components at harmonics of the rf-bias frequency become more significant, $V_b(t)$ becomes less sinusoidal, and an increase is observed in its dc component. The changes in $V_b(t)$ are explained by the nonlinear current-voltage relations of the sheath adjacent to grounded cell surfaces. The rf current flowing from the electrode (or from the inductive source) through the plasma to grounded cell surfaces produces rf and dc voltages across this sheath, which contribute to the plasma potential $V_b(t)$. Indeed, $V_b(t)$ is nearly equal to the ground sheath voltage, as described in the next section.

C. Sheath voltages

The measurements described in the previous sections provide sufficient information to characterize two different regions of the discharge. As shown in Fig. 4, one region extends from the powered electrode to the wire probe (not

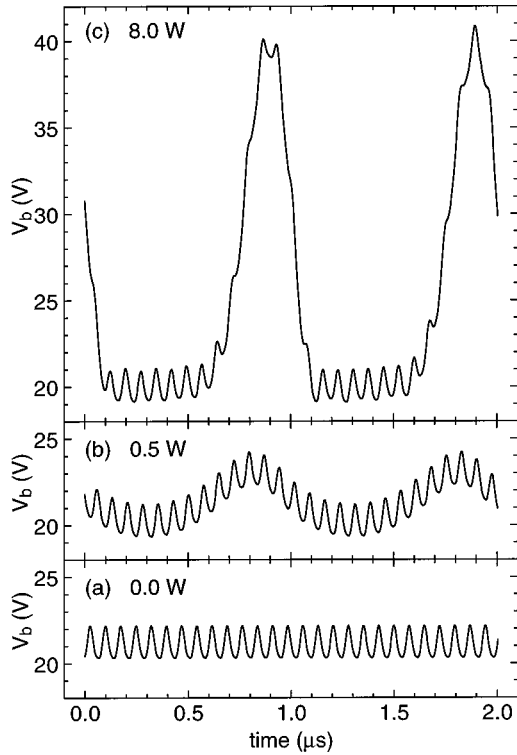


FIG. 3. Wave forms of the plasma potential at the center of the discharge, $V_b(t)$, at an inductive source power of 120 W, rf-bias frequency 1 MHz, and rf-bias powers (P_{pe}) of (a) 0.0 W, (b) 0.5 W, and (c) 8.0 W.

including the wire sheath); the other extends from the wire (not including the wire sheath) to the grounded flange that surrounds the inductive source. Because the plasma density falls off rapidly in the radial direction [49,50], it is assumed in Fig. 4 that the rf current injected at the powered electrode flows out of the plasma at the upper flange, returning along the surface of the chamber wall, rather than flowing out of the plasma at the chamber wall or the lower electrode ground shield. Computer simulations [54] support this assumption. The current through the top region is therefore $I_{ge}(t) = I_{pe}(t) - I_x(t)$, where $I_x(t)$ is the small (~ 1 mA) current drawn by the wire probe. The voltage across the two regions, $V_{ps}(t)$ and $V_{gs}(t)$, are given by

$$V_{gs}(t) = V_b(t) - L_1 dI_{ge}(t)/dt, \quad (5)$$

$$V_{ps}(t) = V_{pe}(t) - V_b(t) - L_2 dI_{pe}(t)/dt. \quad (6)$$

Values of L_1 and L_2 , the self-inductances of the upper and lower sections of the chamber, are given in Fig. 4. The inductance terms account for the electromotive force (emf) generated by the rf current. The emfs are negligible at 0.1–1 MHz, but they are significant at 10 MHz. The emfs depend on the path taken by the current. If the current takes a path other than that shown in Fig. 4, Eqs. (5) and (6) will be in error. The largest errors arise if all of $I_{pe}(t)$ flows to the ground shield of the powered electrode. In that (unlikely) case, no emf terms should be included in Eqs. (5) and (6).

The current injected into the plasma by the coil may also produce emf's, but the magnitude of this current is unknown. Therefore, emf's at the inductive source frequency and its

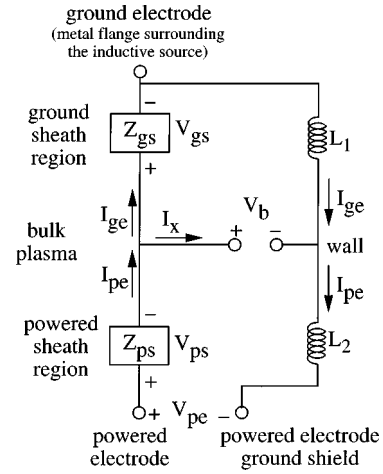


FIG. 4. Electrical representation of the discharge. The discharge is divided into two regions: the region below the wire probe, called the powered sheath region, with voltage drop V_{ps} and impedance Z_{ps} , and the region above the wire probe, called the ground sheath region, with voltage drop V_{gs} and impedance Z_{gs} . The portion of the chamber above the wire probe has a self-inductance L_1 , and the portion of the chamber below the wire probe has a self-inductance L_2 . The values $L_1 = 12$ nH and $L_2 = 20$ nH were obtained from geometrical estimates in which the chamber and ground shields were approximated as a set of coaxial cylinders and chamber flanges were neglected.

harmonics cannot be calculated. Consequently, components at those frequencies are not included in the calculation of $V_{ps}(t)$ and $V_{gs}(t)$ wave forms.

For simplicity, $V_{ps}(t)$ is called the powered electrode sheath voltage and $V_{gs}(t)$ the ground sheath voltage, although, strictly speaking, they contain contributions from the plasma as well as the sheaths. The rf voltage drop across the plasma, measured by mounting the wire probe on a manipulator and moving it through the plasma in the axial direction, was typically only 0.1 V, and at most 2 V, even at hundreds of volts of rf bias. Langmuir probes measure a dc voltage drop of ~ 5 V, in the axial direction, from the center of the plasma to the powered electrode or to the quartz window [49,50]. This drop is included in both $V_{ps}(t)$ and $V_{gs}(t)$. Langmuir probes also measure a radial dc voltage drop $V_r \approx 6$ V across the plasma [49,50], which is included in $V_{gs}(t)$, since the grounded flange of the inductive source that acts as the ground electrode extends only to the outer edge of the quartz window, not to the radial center of the discharge.

Plots of $V_{ps}(t)$ and $V_{gs}(t)$ are shown in Fig. 5. At low rf bias, in Fig. 5(a), $V_{ps}(t)$ and $V_{gs}(t)$ are roughly sinusoidal. At higher rf-bias amplitude, components at harmonics of the rf-bias frequency become more significant, and $V_{ps}(t)$ and $V_{gs}(t)$ take the shape of clipped sinusoids: they are roughly sinusoidal for part of the rf cycle and clipped at a roughly constant baseline for the remainder of the cycle. The baseline voltages do not vary much as the rf-bias power is increased; rather, they remain within a few volts of V_{psf} and V_{gsf} , the dc amplitudes of $V_{ps}(t)$ and $V_{gs}(t)$ measured at zero rf bias, given in Table I.

The sheath voltage wave forms are not symmetric. The relative amplitudes of $V_{ps}(t)$ and $V_{gs}(t)$ vary with conditions, as illustrated by Fig. 5 and by Fig. 6, which plots V_{ps1}

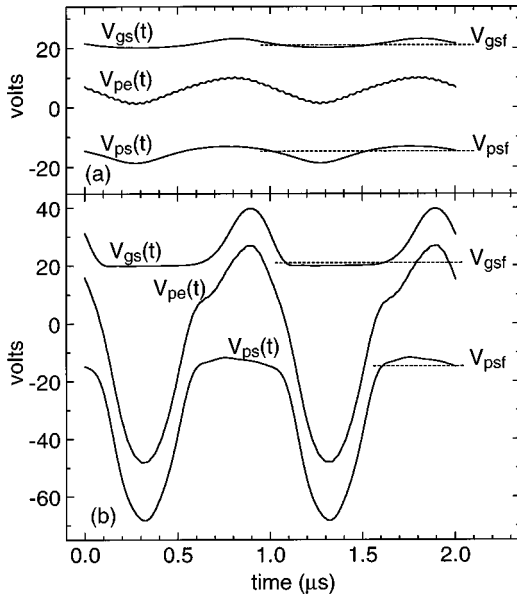


FIG. 5. Wave forms of the voltage across the ground sheath region, $V_{gs}(t)$, the voltage across the powered sheath region, $V_{ps}(t)$, and, for comparison, the voltage on the rf-powered electrode, $V_{pe}(t)$, at an inductive source power of 120 W, rf-bias frequency 1 MHz, and rf-bias powers (P_{pe}) of (a) 0.5 W, and (b) 8.0 W. Also plotted are V_{gsf} and V_{psf} , values of the dc components of $V_{gs}(t)$ and $V_{ps}(t)$ measured with no applied rf-bias power ($P_{pe} = 0.0$ W).

and V_{gs1} , the amplitude of their components at the rf-bias frequency. At an rf-bias frequency of 10 MHz, shown in Fig. 6(a), the sheath voltages are very asymmetric, with $V_{ps1} \gg V_{gs1}$ and $V_{ps1} \approx V_{pe1}$, where V_{pe1} is the amplitude, at the rf-bias frequency, of the voltage on the powered electrode. As rf frequency, voltage, or source power are reduced, however, the division of voltage becomes more symmetric, as V_{ps1} and V_{gs1} approach each other and each approaches $V_{pe1}/2$.

Rectifying properties of the sheaths, evident in Fig. 5, are better illustrated by Fig. 7, where V_{ps0} and V_{gs0} , the dc amplitudes of the sheath voltages, are plotted against V_{ps1} and V_{gs1} . At low sheath voltages, little or no rectification is observed: V_{ps0} and V_{gs0} remain nearly equal to the values measured at zero rf bias, V_{psf} and V_{gsf} . The magnitude of V_{gsf} is larger than V_{psf} , probably due to the radial drop in dc plasma

potential [49,50] discussed above. Consequently, the dc voltage on the powered electrode, V_{pe0} , is positive at low or zero rf bias, as seen in Figs. 2(b) and 5(a). For V_{ps1} or $V_{gs1} > 3$ V in Fig. 7, rectification is observed: $-V_{ps0}$ and V_{gs0} increase as one increases V_{ps1} and V_{gs1} . Eventually, at high voltages, $-V_{ps0} \approx V_{ps1}$ and $V_{gs0} \approx V_{gs1}$. Although both sheaths provide rectification, the larger rf drop across the powered sheath (evident in Fig. 6) generates a larger dc voltage than the ground sheath, so that V_{pe0} is driven negative as the rf-bias voltage, V_{pe1} , is increased, as seen in Figs. 2(b) and 5.

D. Sheath impedance

From the complex Fourier coefficients of the wave forms $V_{ps}(t)$, $V_{gs}(t)$, $I_{pe}(t)$, and $I_{ge}(t)$, at the rf-bias frequency—denoted V_{ps1} , V_{gs1} , I_{pe1} , and I_{ge1} —one obtains the impedances

$$Z_{ps} = V_{ps1} / I_{pe1}, \quad \text{and} \quad (7)$$

$$Z_{gs} = V_{gs1} / I_{ge1}. \quad (8)$$

Like $V_{ps}(t)$ and $V_{gs}(t)$, Z_{ps} and Z_{gs} contain small contributions from the plasma. Nevertheless, the dominant contributions to Z_{ps} and Z_{gs} are made by the sheaths, so they will be referred to as sheath impedances.

The magnitude $|Z_{ps}|$ and phase ϕ_{ps} of Z_{ps} are plotted against the powered sheath voltage, V_{ps1} , in Figs. 8(a) and 9(a). Two regimes are observed. In the first regime, at low sheath voltage, $|Z_{ps}|$ and ϕ_{ps} are independent of voltage. This regime corresponds to the range of rf-bias voltages where $I_{pe}(t)$ and $V_{ps}(t)$ are approximately sinusoidal, as in Fig. 2 (0.5 W) and Fig. 5(a). An impedance that is independent of voltage and a sinusoidal response to a sinusoidal excitation are indications of linear behavior. Therefore the low-voltage regime could be called the linear regime. Although the sheath is in general nonlinear, any nonlinear device will appear to act linearly if the excitation is sufficiently small. In the second regime, at higher rf-bias voltages, the nonlinearity of the sheath is evidenced by changes in $|Z_{ps}|$ and ϕ_{ps} with voltage, and by the nonsinusoidal wave forms and rectification observed in Fig. 2 (8.0 W) and Fig. 5(b). In the high-voltage, nonlinear regime, $|Z_{ps}|$ increases with voltage, and it decreases as the rf-bias frequency increases. In both regimes, $|Z_{ps}|$ falls with increasing inductive source power. The phase

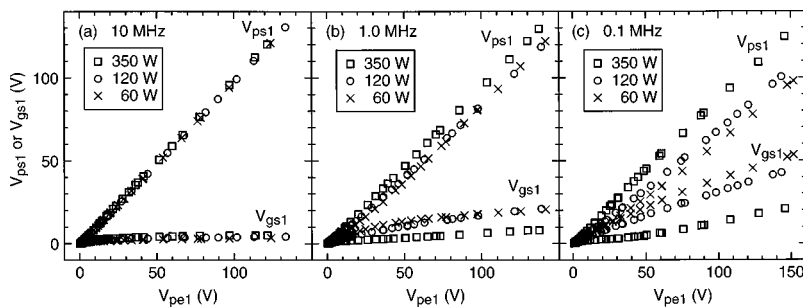


FIG. 6. Amplitudes of sheath voltages for rf-bias frequencies of (a) 10 MHz, (b) 1.0 MHz, and (c) 0.1 MHz, for inductive source powers of 60, 120, and 350 W, and varying rf-bias amplitudes, indicated on the x axis by V_{pe1} , the amplitude of the fundamental component (i.e., the component at the rf-bias frequency) of the voltage on the powered electrode, $V_{pe}(t)$. On the y axis, V_{ps1} and V_{gs1} are the amplitudes of the fundamental components of $V_{ps}(t)$, the voltage across the powered sheath region, and $V_{gs}(t)$, the voltage across the ground sheath region. V_{ps1} and V_{gs1} do not necessarily add to V_{pe1} because of phase differences and because of the emf terms in Eqs. (5) and (6).

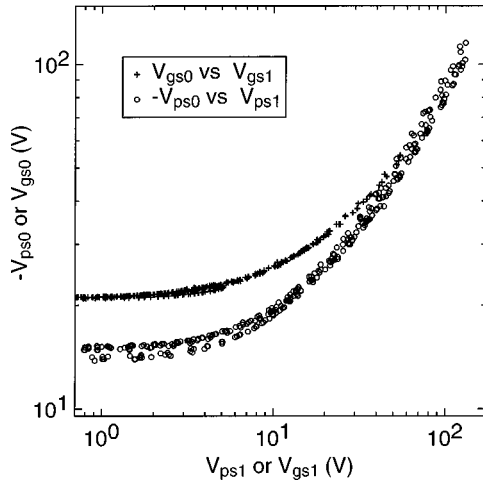


FIG. 7. The dc amplitudes, V_{ps0} and V_{gs0} , of the powered sheath voltage and the ground sheath voltage plotted against V_{ps1} and V_{gs1} , the amplitude of their components at the rf-bias frequency. Data from all rf-bias frequencies and all inductive source powers are plotted.

ϕ_{ps} is resistive (near 0°) at low voltages, low frequencies, and high inductive source powers, but it starts to approach capacitive phases (-90°) as the rf-bias frequency or voltage is increased, or as the source power is decreased.

Similar behavior is observed in Figs. 8(b) and 9(b), which plot the magnitude $|Z_{gs}|$ and phase ϕ_{gs} of the ground sheath impedance, as a function of ground sheath voltage V_{gs1} . A linear regime at low sheath voltage and a nonlinear regime at high sheath voltage are both observed, with one exception: at 10 MHz, when the discharge is quite asymmetric [see Fig. 6(a)], V_{gs1} remains so small that only the linear regime is observed. Compared to ϕ_{ps} , ϕ_{gs} is in general more capacitive (closer to -90°) and the transition of ϕ_{gs} to capacitive phases starts at lower frequencies, higher inductive source powers, and lower voltages. At 10 MHz, ϕ_{gs} is capacitive

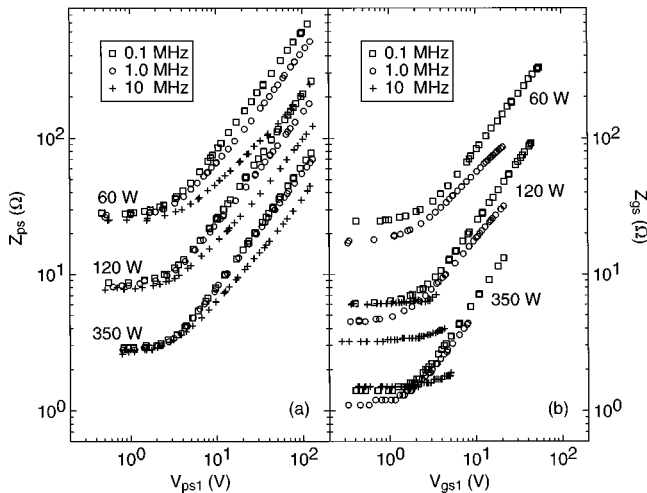


FIG. 8. Magnitude of the impedance (at the rf-bias frequency) of (a) the powered electrode sheath Z_{ps} and (b) the ground sheath Z_{gs} as a function of V_{ps1} and V_{gs1} , the amplitudes (at the rf-bias frequency) of the respective sheath voltages, for rf-bias frequencies of 0.1, 1.0, and 10 MHz, and inductive source powers of (top to bottom) 60, 120, and 350 W.

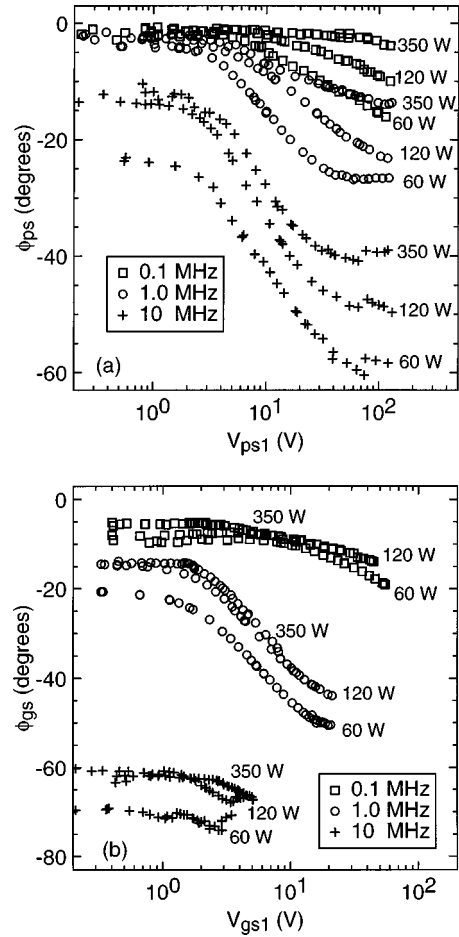


FIG. 9. Phase of the impedance (at the rf-bias frequency) of (a) the powered electrode sheath ϕ_{ps} and (b) the ground sheath ϕ_{gs} as a function of V_{ps1} and V_{gs1} , the amplitudes (at the rf-bias frequency) of the respective sheath voltages, for rf-bias frequencies of 0.1, 1.0, and 10 MHz, and inductive source powers of 60, 120, and 350 W.

even in the linear, low-voltage regime, while ϕ_{ps} is largely resistive. It will be shown in Sec. V that the trend to capacitive impedances at the ground sheath is the cause of the asymmetry of the discharge at high frequencies evident in Fig. 6.

E. Power

The total power flowing at the powered electrode, P_{pe} , was obtained from the Fourier components of $I_{pe}(t)$ and $V_{pe}(t)$, the current and voltage at the powered electrode. The power associated with each Fourier frequency was calculated separately, and then the contributions from all frequencies were summed,

$$P_{pe} = \frac{1}{2} \sum_i |V_{pei}| |I_{pei}| \cos \phi_{pei}, \quad (9)$$

where V_{pei} and I_{pei} are the components of $V_{pe}(t)$ and $I_{pe}(t)$ at the i th frequency, and ϕ_{pei} is the phase of V_{pei} relative to I_{pei} . Up to eight harmonics of the rf-bias frequency were included in the sums. Up to three harmonics of the inductive source frequency were also included, but they made negligible contributions (<10 mW). Many terms in the sum were negative, which indicates that signals generated by the sheaths (or the inductive source) were propagating out of the

plasma, past the electrode, to be dissipated in the rf amplifier or in parasitic resistances. The contribution at ω , the rf-bias frequency, was always positive, with a magnitude 1.00 to 1.14 times *larger* than the total power. The contribution at 2ω had a magnitude of 0–13 % of the total power, and was always negative or zero. Harmonics at frequencies higher than 2ω each contributed less than 3% of the total power. These results differ from previous work with lower-density plasmas, in which no significant power was dissipated at harmonic frequencies [2,53].

Similarly, P_{ps} , the power dissipated in the powered electrode sheath, and P_{gs} , the power dissipated in the ground electrode sheath, were obtained from

$$P_{ps} = \frac{1}{2} \sum_i |V_{psi}| |I_{pei}| \cos \phi_{psi}, \quad (10)$$

and

$$P_{gs} = \frac{1}{2} \sum_i |V_{gsi}| |I_{gei}| \cos \phi_{gsi}, \quad (11)$$

where V_{psi} , V_{gsi} , and I_{gei} are the components of $V_{ps}(t)$, $V_{gs}(t)$, and $I_{ge}(t)$ at the i th frequency, ϕ_{psi} is the phase of V_{psi} relative to I_{pei} , and ϕ_{gsi} is the phase of V_{gsi} relative to I_{gei} . Values for P_{ps} ranged from 51% to 98% of the total power, P_{pe} . Thus, the division of power between the two sheaths ranged from nearly symmetric ($P_{ps} \approx P_{gs}$) to extremely asymmetric ($P_{ps} \gg P_{gs}$). Greater symmetry was obtained at lower rf-bias frequency and lower inductive source power.

In Fig. 10, P_{ps} and P_{gs} are plotted against V_{ps0} and V_{gs0} , the dc voltage drops across the respective sheaths. The functional dependence of P_{ps} on V_{ps0} (to be discussed in Sec. IV C below) and P_{gs} on V_{gs0} , were quite similar. Nevertheless, for most conditions, $V_{gs0} \ll V_{ps0}$ and thus $P_{ps} \ll P_{gs}$. Thus the asymmetric division of voltage observed in Fig. 6 is the cause of the asymmetric division of power.

F. Ion current

To measure the total current of positive ions at the powered electrode, the rf amplifier was replaced by a dc power supply and a dc ammeter, as shown in Fig. 1. If a negative dc voltage is applied to the electrode, electrons from the plasma that would have reached the electrode begin to be repelled. At sufficiently negative dc voltages, no plasma electrons are collected by the electrode, so the dc current measured by the ammeter saturates, as shown in Fig. 11. The saturation current is taken to be the total ion current at the electrode, I_0 . Data in Fig. 11 show that I_0 is roughly proportional to the inductive source power.

In previous measurements performed at electrodes that were simultaneously powered by rf and dc power supplies, in low-density, parallel-plate cells, the flat ion saturation current region shown by Fig. 11 was not observed [39,46,47]. Instead, the dc current-voltage curve had a nonzero slope in the ion saturation region, and an extrapolation of the curve was required. Here, no extrapolation is required, and errors inherent in the extrapolation are avoided. The accuracy of the ion current measurement is limited instead by secondary

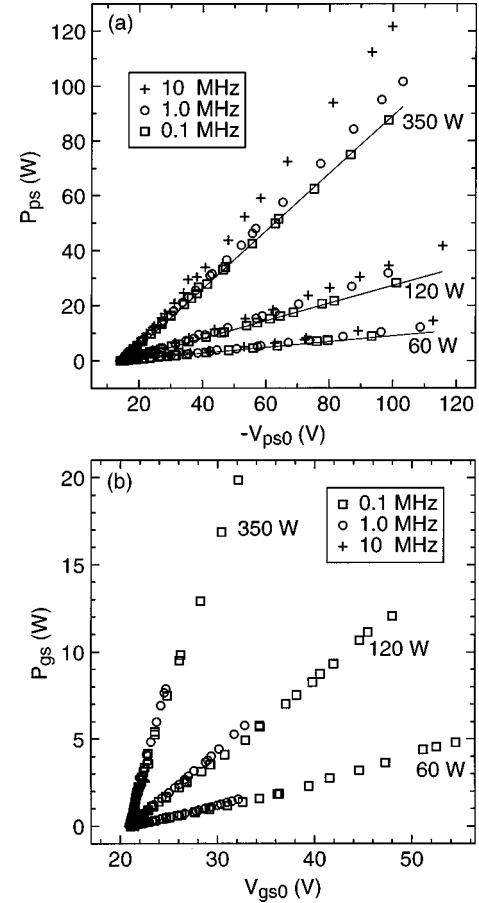


FIG. 10. Total power (summed over all frequencies) of (a) the powered electrode sheath P_{ps} and (b) the ground sheath P_{gs} as a function of V_{ps0} and V_{gs0} , the dc amplitudes of the respective sheath voltages, for rf-bias frequencies of 0.1, 1.0, and 10 MHz, and inductive source powers of 60, 120, and 350 W. The solid lines in (a) are model predictions obtained from Eq. (33).

electrons, which are counted as ions. The resulting systematic error in I_0 is estimated to be $\leq 9\%$, based on measurements of the secondary electron yields of Ar^+ ions at aluminum surfaces [55,56].

Values of I_0 are reported in Table I. They are mean values, averages of measurements repeated periodically during the experiments. No systematic variations of I_0 with time were observed. Random variations had a standard deviation of 1%.

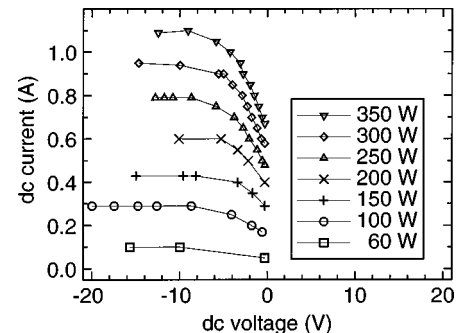


FIG. 11. The dc current at the lower electrode as a function of the dc voltage imposed on the lower electrode for inductive source powers of 60–350 W, with no rf-bias applied.

In the remainder of this paper, the measurements of sheath electrical properties described above are compared to models. The powered electrode sheath is treated first. Then, in Sec. V, the ground sheath is discussed.

IV. ANALYSIS OF THE POWERED ELECTRODE SHEATH

A. Current wave forms

Predictions for current and voltage wave forms are provided by several sheath models. Low-frequency, “quasi-static” sheath models [7,8,29,30] predict that the current flowing through a sheath, $I(t)$, is given by the diode equation

$$I(t) = -I_0 + I_{e0} \exp[-V_s(t)/T_e]. \quad (12)$$

The first term, $-I_0$, is the ion current. It is negative, corresponding to a flow of positive ions from the plasma to the electrode. Negative ions in the plasma are not collected at the electrode; they are reflected back into the plasma by the electric field in the sheath. Most of the plasma electrons are also reflected. To be transmitted across the sheath, plasma electrons must have sufficient kinetic energy to surmount the potential barrier presented by $V_s(t)$, the time-varying sheath voltage (defined here as the voltage in the plasma relative to the voltage on the electrode). For a Maxwell-Boltzmann distribution of plasma electrons at temperature T_e (in volts), the current carried by transmitted electrons is given by the second term in Eq. (12). The prefactor I_{e0} depends on the electron temperature and density. Usually I_{e0} and T_e are assumed to be time independent, as is I_0 .

At the point where electrons are reflected, there is a steep drop in the electron density. In the sheath, that is, in the region between this steep drop and the electrode, the electron density is much lower than the positive ion density. Consequently, the sheath contains a net positive charge $Q(t)$, which is compensated by a negative charge $-Q(t)$ on the electrode surface. As the sheath voltage $V_s(t)$ varies over an rf cycle, the sheath charge and surface charge both vary, so that a charging current dQ/dt flows in the electrode’s electrical connections and through the plasma, and a displacement current flows across the sheath. At low frequencies, the displacement current can be neglected, and Eq. (12) is valid. At high frequencies, when ions cannot respond to the rf fields, the total current, including the displacement current, is [2]

$$I(t) = -I_0 + I_{e0} \exp[-V_s(t)/T_e] + [\varepsilon_0 A/W(t)] dV_s/dt, \quad (13)$$

where ε_0 is the permittivity of vacuum, A is the electrode area, and $W(t)$ is the time-varying width of the sheath, which can be obtained from numerical [35,39], or analytical [31,32] solutions.

Models have also been proposed for the intermediate frequency regime, in which the displacement current cannot be neglected, but the ions are still wholly or partly able to follow the rf fields [12,42,43]. Under certain conditions, discussed below, the total current predicted by these models can be expressed as

$$I(t) = -I_0 + I_{e0} \exp[-V_s(t)/T_e] + [k\varepsilon_0 A/W(t)] dV_s/dt, \quad (14)$$

where k is a constant, $W(t)$ is the sheath width obtained from the Child-Langmuir law [57],

$$W(t) = \frac{2}{3} (2e/m_i)^{1/4} (\varepsilon_0 A/I_0)^{1/2} [V_s(t)]^{3/4}, \quad (15)$$

and e/m_i is the charge to mass ratio of the positive ions. The value of k varies from model to model. In the limit $V_s(t) \gg T_e$, the current-voltage relations of Refs. [42, 43] are equivalent to Eqs. (14) and (15) with $k=1/3$. In Ref. [12], the value of k is not completely specified. If the Debye length used in that paper is taken to be the Debye length at the boundary between the plasma and the sheath, and if the ion velocity at that boundary is equal to the Bohm velocity, then a value of $k=2^{1/4}$ is obtained.

To compare model predictions with experiment, model current wave forms $I(t)$ were calculated by substituting $V_s(t) = -V_{ps}(t)$ into Eqs. (14) and (15). The parameters I_0 , I_{e0} , T_e , and k were adjusted to fit the measured current waveform $I_{pe}(t)$. Figure 12 shows a comparison between model and measured current wave forms. Also plotted are the experimental $V_{ps}(t)$ wave form used in the calculation and separate calculated wave forms for the conduction current terms,

$$I_c(t) = -I_0 + I_{e0} \exp[-V_s(t)/T_e], \quad (16)$$

and the displacement current term,

$$I_d(t) = [k\varepsilon_0 A/W(t)] dV_s/dt. \quad (17)$$

In the figure, the conduction current $I_c(t)$ consists of a constant baseline (which is the ion current, $-I_0$) and a pulse of electron current. When the magnitude of sheath voltage is large, the electron current is negligible, thus $I_c(t) = -I_0$. When the magnitude of the sheath voltage is small, the electron current is large and very sensitive to the sheath voltage. This sensitivity arises from the exponential dependence in Eq. (16). The exponential dependence produces the “clipping” of the sheath voltage wave form, as in a diode.

In contrast, over the portion of the cycle where the sheath voltage is clipped, the displacement current $I_d(t)$ is small, because dV_{ps}/dt is small. Over the remainder of the cycle, $V_{ps}(t)$ is roughly parabolic, so dV_{ps}/dt and $I_d(t)$ are both roughly linear. The resulting shape of the displacement current wave form is similar to previous calculations [42,43]. When the rf-bias frequency is lowered from 1.0 MHz (in Fig. 12) to 100 kHz, shown in Fig. 13, the shape of the displacement current $I_d(t)$ does not change, but it becomes a much smaller fraction of the total current. Therefore, the conduction current $I_c(t)$ is nearly equal to the total current $I(t)$. At 10 MHz, as shown in Fig. 14, $I_d(t)$ is much larger. The shape of $I_d(t)$ in Fig. 14 is similar to Fig. 12, except that the fraction of the rf cycle over which $I_d(t) \approx 0$ [and over which $V_{ps}(t)$ is clipped] is shorter.

The fitting procedure was performed on wave forms distributed throughout the experimental space. Excellent fits were obtained for most conditions, although at 10 MHz, fits obtained at high sheath voltages (e.g., Fig. 14) were not as good. Values of I_0 obtained from the fits agreed with the dc

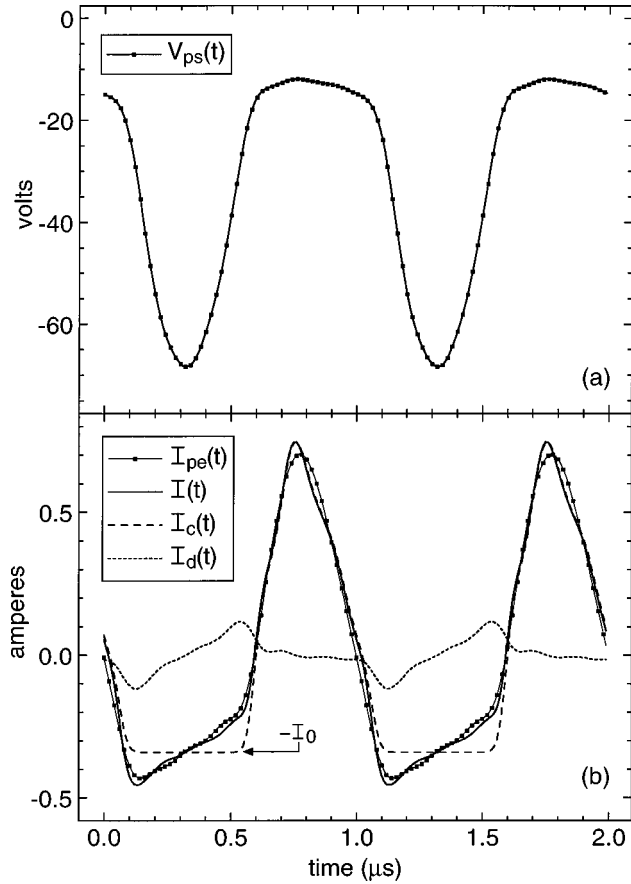


FIG. 12. Analysis of wave forms at the powered electrode sheath, measured at 1.0 MHz rf-bias frequency and an inductive source power of 120 W. (a) Experimental wave form for the sheath voltage, $V_{ps}(t)$. (b) Experimental current wave form $I_{pe}(t)$ compared to model wave forms $I(t)$, $I_c(t)$, and $I_d(t)$, where $I(t)$ is the total current, $I_c(t)$ is the conduction current, and $I_d(t)$ is the displacement current. Model wave forms were obtained from Eqs. (14)–(17) with $V_s(t) = -V_{ps}(t)$, $I_0 = 0.34$ A, $I_{e0}/I_0 = 148$, $k = 1.0$, and $T_e = 3.1$ V.

measurements in Table I: they differed by less than 10% (usually by $<3\%$). Values of T_e ranged from 2.6 to 3.4 V (usually 2.8–3.0 V). Comparison with previously reported electron temperatures [49,50] is complicated because measured electron energy distribution functions (EEDF's) are non-Maxwellian [50]. The low-energy portion of the EEDF is not relevant, because low-energy electrons do not contribute to the electron conduction current in Eqs. (14) and (16); they are instead reflected back into the plasma. Only electrons with energies near $-eV_{psf}$ (~ 15 eV, see Table I) or higher contribute to the electron conduction current. At these high energies, the slope of electron energy probability functions measured in argon at 1.0–2.6 Pa (7.6–20 mTorr) [50,58] is consistent with an electron temperature of 2.9 V. Therefore, one can conclude that, if the non-Maxwellian EEDF is accounted for, values of T_e obtained from the fitting procedure agree with Langmuir probe measurements.

Values of I_{e0}/I_0 obtained from the fits ranged from 70 to 190. These values differ from predicted values, because of the non-Maxwellian EEDF. It should be noted that I_{e0} is not an independent parameter. Once trial values for T_e and I_0 are selected by the fitting procedure, the factor I_{e0} is fixed by the

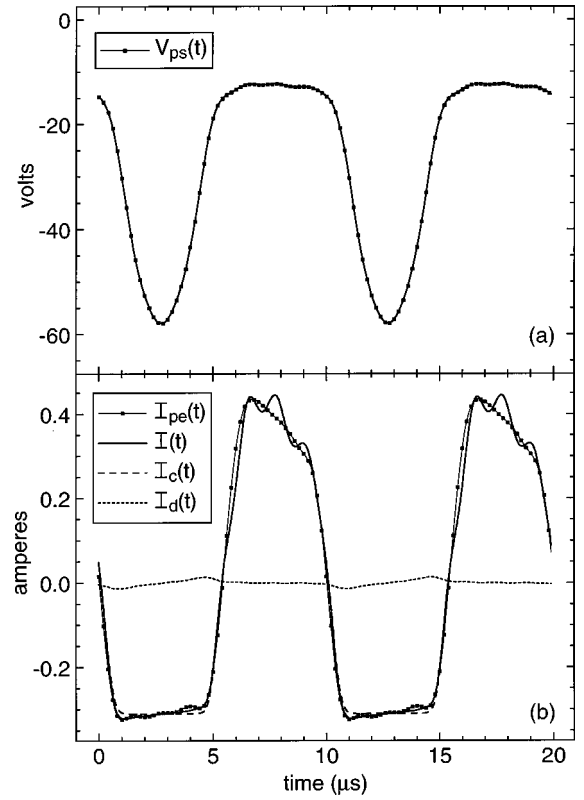


FIG. 13. Comparison of experimental and model wave forms at the powered electrode sheath, measured at 100 kHz rf-bias frequency and an inductive source power of 120 W. The wave forms are defined in Fig. 12. Model wave forms were obtained from Eqs. (14)–(17) with $V_s(t) = -V_{ps}(t)$, $I_0 = 0.31$ A, $I_{e0}/I_0 = 114$, $k = 1.3$, and $T_e = 3.2$ V.

condition that the model current, averaged over one rf cycle, is zero.

Values of k obtained from the fitting procedure varied systematically with rf-bias frequency, ranging from 1.0 to 1.3 at 100 kHz, 0.9 to 1.2 at 1 MHz, and 0.5 to 1.0 at 10 MHz (excepting some wave forms at 100 kHz, where the displacement current component was so small that values of k could not be reliably determined). These results are not in agreement with Refs. [42,43], which predict $k = 1/3$. The value of $k = 2^{1/4}$, obtained from Ref. [12], as described above, is in better agreement with experimental values. The disagreement with Refs. [42,43] may be attributed to failures in those models. Indeed, those models do not appear to be self-consistent; in them, the ion continuity equation is violated in the sheath. Also, the models use the Child-Langmuir law, Eq. (15), which assumes that the ions are in equilibrium with the rf field. At high rf frequencies the ions will not be in equilibrium. Finally, Refs. [42,43] assume that the ion current is constant in time, but this assumption is not valid at all frequencies [59].

B. Impedance

Because the conduction current and displacement current flow in parallel through the sheath, it is helpful to represent the sheath impedance as a conductance G_{ps} in parallel with a capacitance C_{ps} . In terms of $|Z_{ps}|$ and ϕ_{ps} , the magnitude and phase of the sheath impedance,

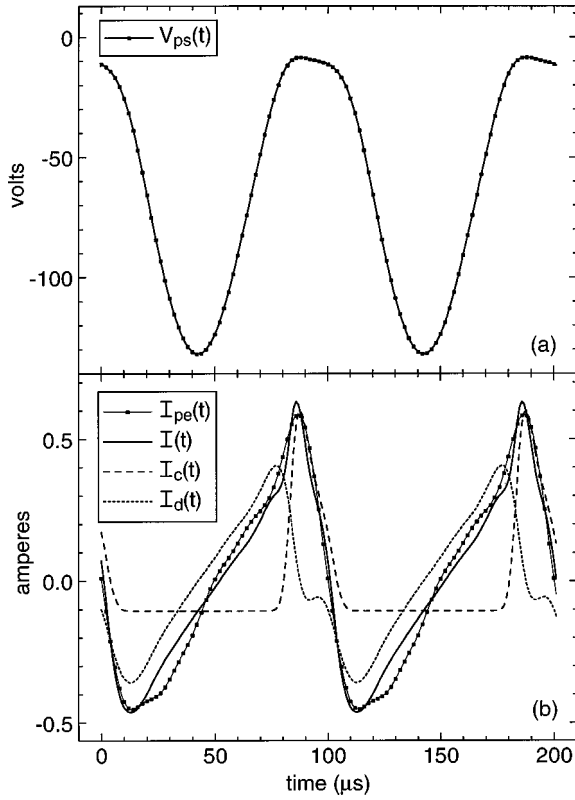


FIG. 14. Comparison of experimental and model wave forms at the powered electrode sheath, measured at 10 MHz rf-bias frequency and an inductive source power of 60 W. The wave forms are defined in Fig. 12. Model wave forms were obtained from Eqs. (14)–(17) with $V_s(t) = -V_{ps}(t)$, $I_0 = 0.105$ A, $I_{e0}/I_0 = 100$, $k = 0.5$, and $T_e = 3.1$ V.

$$G_{ps} = \text{Re}(1/Z_{ps}) = |Z_{ps}|^{-1} \cos \phi_{ps}, \quad \text{and} \quad (18)$$

$$\omega C_{ps} = \text{Im}(1/Z_{ps}) = -|Z_{ps}|^{-1} \sin \phi_{ps}. \quad (19)$$

If the sheath were linear, it would, when excited by a voltage $V_{s1}e^{i\omega t}$, pass a conduction current $I_{c1}e^{i\omega t}$ and a displacement current $iI_{d1}e^{i\omega t}$ (where V_{s1} , I_{c1} , and I_{d1} are real). Its conductance,

$$G = I_{c1}/V_{s1}, \quad (20)$$

would depend on the amplitude of the conduction current I_{c1} , but not on the displacement current I_{d1} , while its capacitance would depend on I_{d1} , but not I_{c1} :

$$\omega C = I_{d1}/V_{s1}. \quad (21)$$

For a nonlinear device, Eqs. (20) and (21) are not necessarily valid [39,60], but G and ωC , as well as the equivalent parallel resistance $1/G$ and the equivalent parallel reactance $1/(\omega C)$ are still useful parameters.

In Fig. 15, experimental values of the equivalent parallel resistance $1/G_{ps}$ are plotted and compared with model predictions. The prediction at low sheath voltages was obtained by noting that, at low voltages,

$$V_s(t) \approx V_f + V_{s1}e^{i\omega t}, \quad (22)$$

where V_f is the voltage at which $I_c(t)$ in Eq. (16) is zero,

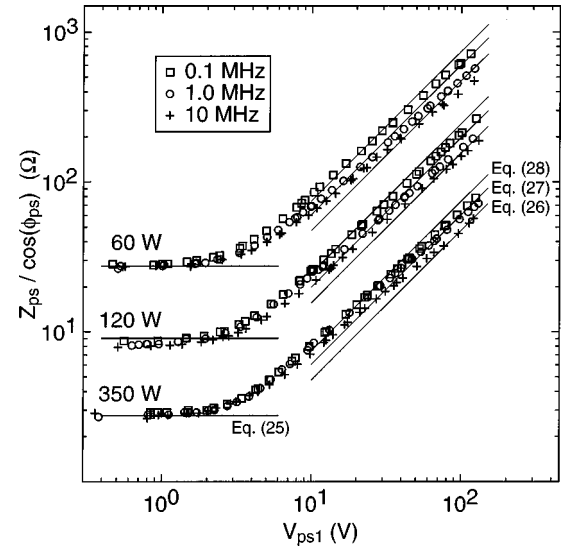


FIG. 15. The equivalent parallel resistance of the powered sheath, $1/G_{ps} = |Z_{ps}|/\cos \phi_{ps}$, as a function of V_{ps1} , the amplitude at the rf-bias frequency of the voltage across the powered electrode sheath, for rf-bias frequencies of 0.1–10 MHz and inductive source powers (P_L) of 60–350 W. Solid lines show the equivalent parallel resistance $1/G$ obtained from model predictions, Eqs. (25)–(28). The model calculations used values of I_0 from Table I.

$$V_f = T_e \ln(I_{e0}/I_0). \quad (23)$$

Approximating $I_c(t)$ as a Taylor series expansion about the voltage V_f , and keeping only the first nonzero term:

$$I_c(t) \approx \left. \frac{dI_c}{dV_s} \right|_{V_s=V_f} V_{s1}e^{i\omega t} = \frac{I_0}{T_e} V_{s1}e^{i\omega t}. \quad (24)$$

Using Eq. (20), one obtains

$$1/G = T_e/I_0. \quad (25)$$

This equation is plotted in Fig. 15, using values of I_0 from Table I, and a single value of the electron temperature $T_e = 2.9$ V. As discussed above, this value is consistent with measurements of the slope of the EEDF at electron energies ≥ 15 eV. The prediction, Eq. (25), agrees with the experimental data at sheath voltages < 2 V.

Values of $1/G_{ps}$ at higher voltages depend on the shape of the $I_c(t)$ wave form. If $I_c(t)$ consists of a short pulse of electron current riding on a constant baseline $\approx I_0$, then I_{c1} can be shown [2] to obey $I_{c1} \approx 2I_0$. Thus, using Eq. (20),

$$1/G = V_{s1}/I_{c1} \approx (1/2)V_{s1}/I_0. \quad (26)$$

If $I_c(t)$ is a half-wave rectified wave form with a baseline equal to I_0 , then

$$1/G = V_{s1}/I_{c1} = (2/\pi)V_{s1}/I_0. \quad (27)$$

Finally, if $I_c(t)$ is a symmetric square wave with a baseline equal to I_0 , then

$$1/G = V_{s1}/I_{c1} = (\pi/4)V_{s1}/I_0. \quad (28)$$

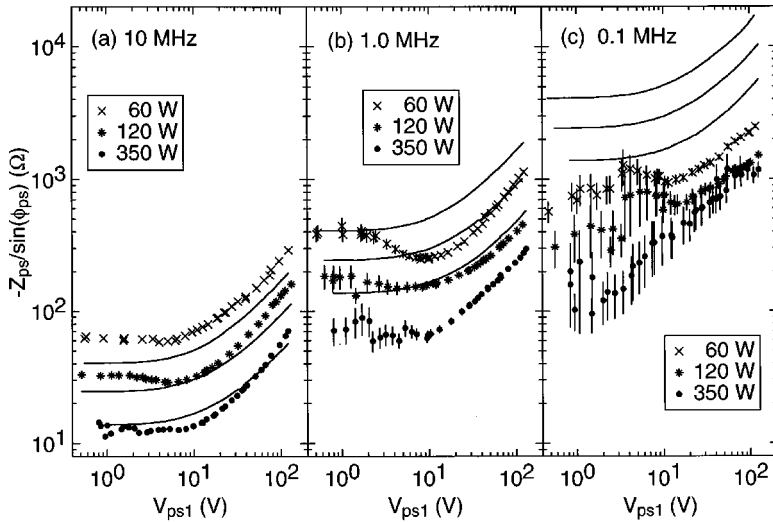


FIG. 16. The equivalent parallel reactance of the powered sheath, $1/(\omega C_{ps}) = -|Z_{ps}|/\sin \phi_{ps}$, as a function of V_{ps1} , the amplitude of the voltage across the powered electrode sheath, for rf-bias frequencies of (a) 10 MHz, (b) 1 MHz, and (c) 0.1 MHz and inductive source powers (P_L) of 60–350 W. Solid lines show model predictions [obtained by substituting Eq. (30) into Eq. (29)] plotted for each value of P_L , using values of I_0 from Table I.

Plots of these equations appear as parallel lines on the log-log axes of Fig. 15. Data from 0.1 MHz agree best with Eq. (28), since at 0.1 MHz $I_c(t)$ resembles a square wave (Fig. 13). At 1.0 MHz, $I_c(t)$ resembles a half-wave rectified wave form (Fig. 12), hence Eq. (27) is in best agreement with the data. At 10 MHz, $I_c(t)$ resembles a sharp pulse at high voltages (Fig. 14) but a half-wave rectified wave form at intermediate voltages. Thus 10-MHz data agree best with Eq. (26) at high voltages and Eq. (27) at intermediate voltages. Deviations between the model predictions and the data are observed because $I_c(t)$ deviates from the ideal wave form shapes assumed in Eq. (26)–(28).

The equivalent parallel reactance of the powered electrode sheath, $1/(\omega C_{ps})$, obtained from Eq. (19), is plotted in Fig. 16. Error bars show the uncertainty in $1/(\omega C_{ps})$ produced by a $\pm 0.5^\circ$ uncertainty in ϕ_{ps} . At conditions where $\phi_{ps} \approx 0$ (see Fig. 9) the uncertainty in $1/(\omega C_{ps})$ is large. At these conditions, the displacement current is small compared to the conduction current, so it is difficult to determine $1/(\omega C_{ps})$ precisely.

Figure 16 also shows predictions from Ref. [40]. There, the sheath parallel reactance is set equal to

$$1/(\omega C) = W/(\omega \epsilon_0 A), \quad (29)$$

which is the reactance of a parallel plate capacitor of the same area as the electrode (A) and a plate separation W , where W is obtained by inserting the dc sheath voltage V_{s0} into the Child-Langmuir law, i.e.,

$$W = \frac{2}{3} (2e/m_i)^{1/4} (\epsilon_0/J_0)^{1/2} V_{s0}^{3/4}. \quad (30)$$

There are some similarities in the behavior of the data and the model, but there are also significant differences, especially at 0.1 MHz. Predictions from other models do not agree any better with the data. For example, at high sheath voltages, the high-frequency model of Lieberman [31] is equivalent to Eqs. (29) and (30), if the factor $\frac{2}{3}$ is replaced by 0.88. Changing the prefactor to 0.88 does not, however, consistently improve the agreement with experiment. In the low-voltage ($V_{s1} \rightarrow 0$) limit, V_{s0} approaches a constant value V_f given in Eq. (23), and models [42,43] predict that

$$1/(\omega C) = k_f \lambda_D / (\omega \epsilon_0 A), \quad (31)$$

where k_f is a dimensionless constant, λ_D is the Debye length

$$\lambda_D = (n_0 e / \epsilon_0 T_e)^{-1/2}, \quad (32)$$

and n_0 is the electron density at the position (between the plasma and the sheath) at which the ion velocity equals the Bohm velocity. The value of k_f depends on V_f , which in turn depends on the ion mass. For argon, models [42,43] yield $V_f = 5.2 T_e$, and $k_f = 5.0$. In contrast, a value of $k_f = 2.3$ is obtained from the low-voltage ($V_{s1} \rightarrow 0, V_{s0} \rightarrow V_f$) limit of Eqs. (29) and (30). Thus, at low sheath voltages, the models of Refs. [42,43] predict higher values of $1/(\omega C)$ —and hence greater deviations from the data—than the model curves shown in Fig. 16.

The disagreement of the models with experiment partly results from an assumption, made by the models that the reactance $1/(\omega C)$ depends solely on the displacement current, as in Eq. (21). For a nonlinear device, however, Eq. (21) is not necessarily valid [39,60]. The electron conduction current given in Eq. (12) may have a component that is out of phase with the voltage, so that it contributes to $1/(\omega C)$ rather than $1/G$. If the ion conduction current varies with time, it too may have components that contribute to $1/(\omega C)$. Because the displacement current decreases as frequency becomes lower, one might expect the conduction current to have a larger effect on $1/(\omega C)$ at low frequencies, causing the disagreement to become worse at low frequencies, as observed. A complimentary situation has been noted in lower-density plasmas [39]. There, the displacement current, which is much larger than the conduction current, has a component that is in phase with the sheath voltage, which makes the sheath parallel resistance $1/G$ smaller than one would predict if one only considered the conduction current.

It should also be noted that Eqs. (20) and (21) neglect the electrons reflected by the sheath. Although a static sheath reflects electrons elastically, a net transfer of energy to electrons reflected from an rf-biased sheath may occur [1,31]. This energy dissipation mechanism, known as stochastic heating, can be represented by a resistance in series with the sheath capacitive reactance. In low-density cells, at low applied voltages, this stochastic resistance is significant, 100 Ω

or more [1,2,61]. In this study, however, due to the higher plasma densities, values of the stochastic resistance obtained using equations from Refs. [1,31] are less than 1Ω , small enough to be neglected in all of the analyses presented above.

C. Power

Reference [40] gives an expression for the power P dissipated by a sheath:

$$P = I_0(V_{s0} - V_f), \quad (33)$$

where V_{s0} is the dc voltage across the sheath and V_f is the value of V_{s0} when no rf bias is applied (or, more precisely, when no rf current flows across the sheath). I_0 is the time-averaged flux of ions (or electrons) collected at the electrode. The first term is the power gained by ions, which are accelerated as they cross the sheath; the second is the power lost by the electrons, which are decelerated as they cross the sheath. If no rf bias is applied, the two terms cancel, and the sheath dissipates no net power. When rf bias is applied, it is rectified by the sheath, producing an increase in V_0 and in the power absorbed by the ions. Electrons, however, are only transmitted when the sheath voltage is near its minimum value, and this minimum remains approximately equal to V_f (see Fig. 5). Therefore the power lost by electrons should remain more or less unchanged, at the value $I_0 V_f$. At high rf bias the second term is small compared to the first, and models often neglect it.

Inserting values of I_0 and V_{psf} from Table I into Eq. (33), predictions for the power dissipation in the powered electrode sheath were obtained. Figure 10(a) shows that the predictions are in excellent agreement with the data at 0.1 MHz. At higher frequencies, P_{ps} still shows a linear dependence and an x intercept of V_{psf} , but it falls above the predicted line. This deviation suggests that an additional power dissipation mechanism is present at higher frequencies. Possible mechanisms include the stochastic heating associated with electrons reflected by the sheath [31] or the launching of a plasma wave. The deviation in Fig. 10(a) could also be explained by the ion current varying with time over an rf cycle, as is predicted at high frequencies [59]. If I_0 is not constant, Eq. (33) is not valid.

V. ANALYSIS OF THE GROUND SHEATH

In this section, the current flow through the ground sheath and the ground sheath impedance are analyzed. A complete, quantitative comparison with models is not possible here, because the dc ion current through the ground sheath was not measured. Nevertheless, the electrical properties of the ground sheath are important. They must be understood if one is to explain observed variations in the asymmetry of the discharge.

A. Ground sheath current wave forms

The current flowing through the ground sheath, $I_{ge}(t)$, is nearly equal to the current flowing through the powered electrode sheath, $I_{pe}(t)$. At any particular time, however, the mechanism of current flow in the sheaths is not the same, because the sheath voltages differ in phase. When the pow-

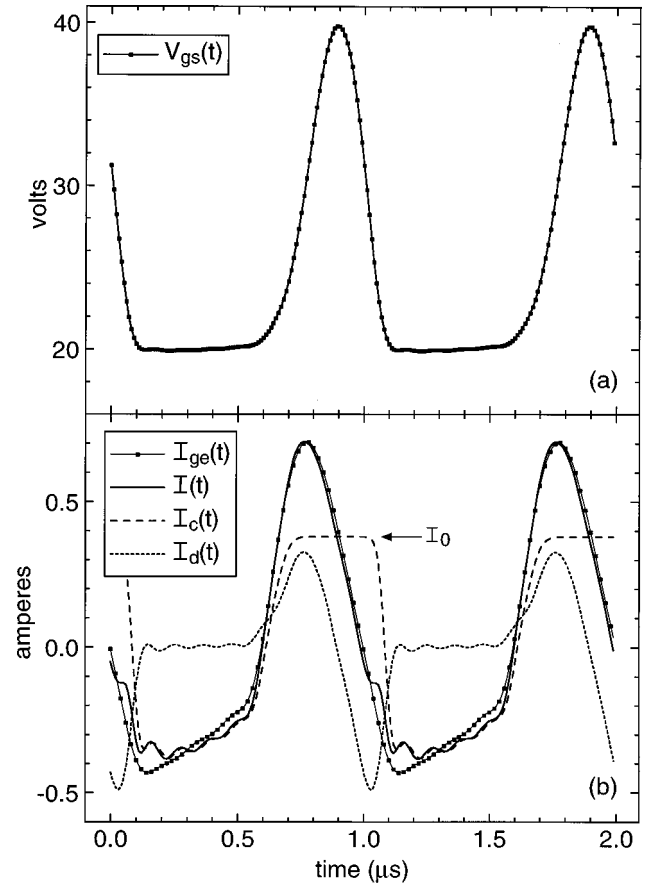


FIG. 17. Analysis of wave forms at the ground sheath, measured at the same conditions as Fig. 12. (a) Experimental wave form for the sheath voltage, $V_{gs}(t)$. (b) Experimental current wave form $I_{ge}(t)$ and model wave forms $I(t)$, $I_c(t)$, and $I_d(t)$ where $I(t)$ is the total current, $I_c(t)$ is the conduction current, and $I_d(t)$ is the displacement current. Model wave forms were obtained from Eqs. (14)–(17) with $V_s(t) = V_{gs}(t) - V_r$, $V_r = 6$ V, $I_0 = 0.38$ A, $I_{e0}/I_0 = 2.10 \times 10^4$, $k = 6.2$, and $T_e = 1.5$ V.

ered sheath voltage $V_{ps}(t)$ is large, the ground sheath voltage $V_{gs}(t)$ is small, and vice versa (see Fig. 5). To investigate current flow in the ground sheath, $V_{gs}(t)$ [or $V_{gs}(t) - V_r$, where V_r is the radial dc voltage drop across the plasma, discussed in Sec. III C] was inserted into Eqs. (14) and (15), which were then fit to the $I_{ge}(t)$ wave form. Wave forms for the conduction current, displacement current, and total current obtained from this fitting procedure are shown in Fig. 17. As in Fig. 12, the conduction current consists of a constant baseline (which is now positive) and a pulse of electron current (now negative). The shape of the displacement current wave form is similar to that of Fig. 12, except for a time shift and a change in polarity. As in Fig. 12, the electron current only flows when the sheath voltage is small, and the displacement current only flows when the sheath voltage (or, more precisely, its time derivative) is large.

The values of I_0 and k obtained from the fit shown in Fig. 17 are larger than the values from Fig. 12, indicating that the effective area of the ground sheath is larger than the area of the powered electrode. In contrast, the value of T_e is smaller. Presumably, electron currents collected at relatively remote grounded surfaces account for the lower value of T_e . Langmuir probe measurements indicate that the electron temperature falls off rapidly in the radial direction [49,50]. There are

no grounded surfaces near the radial center of the discharge, only the quartz window.

B. Ground sheath impedance

At 100 kHz and 1 MHz the behavior of the ground sheath impedance in Figs. 8(b) and 9(b) is quite similar to the behavior of the powered sheath impedance. At 10 MHz, however, Z_{gs} is, at any given sheath voltage, smaller than Z_{ps} . Also, the phase ϕ_{gs} is more capacitive (closer to -90°) than ϕ_{ps} . Even at very low voltages ϕ_{gs} is capacitive, unlike ϕ_{ps} , which has a phase that is resistive (near 0°). This difference is explained by the plasma density in the vicinity of the grounded surfaces being, on average, lower than the plasma density adjacent to the powered electrode. According to Eqs. (18), (19), (25), and (31), a small area element of a sheath will have an impedance phase ϕ given by

$$\tan \phi = (1/k_f)(\omega/\omega_i), \quad (34)$$

where ω_i is the ion plasma frequency,

$$\omega_i = (e^2 n_0 / m_i \epsilon_0)^{1/2}, \quad (35)$$

and n_0 is the positive ion density at the sheath edge, i.e., at the point between the plasma and the sheath where the ion velocity is equal to the Bohm velocity, $(eT_e/m_i)^{1/2}$.

Because $\phi_{ps} \approx 0^\circ$ at low voltages in Fig. 9(a), the ion plasma frequency at the edge of the powered electrode sheath, ω_{ps} , must obey $\omega_{ps} > \omega/k_f$, even at 10 MHz. In contrast, the behavior of ϕ_{gs} in Fig. 9(b) suggests that ω_{gs} , the ion plasma frequency at the edge of the ground sheath, obeys $\omega_{gs} < \omega/k_f$ at 10 MHz. As the rf frequency approaches ω_{gs} from below, the impedance of the ground sheath decreases rapidly, relative to the powered sheath impedance. Consequently, a greater fraction of the fundamental rf-bias voltage, V_{pe1} , will be dropped across the powered sheath, resulting in an increasing asymmetry in V_{ps1} and V_{gs1} as the frequency is increased. The asymmetry is further increased by the nonlinearity of the powered sheath impedance. As the voltage drop across the powered sheath increases, the sheath impedance Z_{ps} increases, causing the powered sheath to draw an even larger fraction of V_{pe1} . This feedback mechanism drives the discharge to a very asymmetric state. Thus at 10 MHz V_{gs} remains small, never leaving the low-voltage, linear region.

At 0.1–1 MHz, $\omega \ll \omega_{gs}$, so the ground sheath is resistive rather than capacitive at low sheath voltages. The observation that the resistive ground sheath allows greater symmetry in V_{ps1} and V_{gs1} can be explained using a spherical shell model (similar to those used by Lieberman [9]) in which ions and electrons diffuse freely in three dimensions, without losing energy, between a powered inner sphere and a grounded, concentric outer sphere. If the sheath at the outer sphere is

capacitive, with the impedance given in Eqs. (29) and (30), its impedance will approach zero as its radius goes to infinity, making the discharge more and more asymmetric. In contrast, the impedance of a resistive sheath, given by Eq. (25), will remain constant as its radius goes to infinity, so the discharge remains symmetric.

Changes in the symmetry of the discharge have important effects on the kinetic energies of ions bombarding the grounded surfaces. These ions are accelerated by the ground sheath voltage. Recent measurements [62] of ion energies at grounded surfaces confirm these predictions, and show that the change in the symmetry of the discharge with frequency is a dominant factor in controlling ion energies.

VI. CONCLUSIONS

Measurements of the rf current and voltage applied to the substrate electrode of a high-density plasma reactor, combined with dc measurements of the ion current at the electrode and wire probe measurements of the plasma potential, enabled a rigorous, quantitative test of models of the electrical properties of the sheath adjacent to the electrode. An equation describing the current-voltage relations of the sheath was presented. The equation includes a conduction current component given by the diode equation, as well as a displacement current component, the magnitude of which is not correctly predicted by existing models. The equivalent parallel conductance of the sheath agrees with simple approximate forms, but the equivalent parallel capacitance of the sheath does not agree with any existing models. At low rf-bias frequency (100 kHz) the power dissipated in the sheath is in agreement with simple expressions for the power absorbed by ions crossing the sheath, but this agreement was not obtained at higher frequencies.

The sheath at grounded surfaces was also studied in detail. The current-voltage relation and the impedance of the ground sheath generally behaved in a manner similar to the sheath at the rf-biased electrode. An exception occurs at the highest rf-bias frequency, 10 MHz. There, because of the differing plasma densities in the vicinity of the two sheaths, the ground sheath has a predominantly capacitive impedance while the powered electrode sheath has a predominantly resistive impedance. This results in a very asymmetric sharing of voltage by the two sheaths, as predicted by spherical shell models of the discharge.

ACKNOWLEDGMENTS

I would like to thank Eric Benck and Axel Schwabedissen for their work assembling and maintaining the high-density plasma cell, and Christian Kendrick for valuable comments on the manuscript.

-
- [1] V. A. Godyak, R. B. Piejak, and B. M. Alexandrovich, IEEE Trans. Plasma Sci. **19**, 660 (1991).
 [2] M. A. Sobolewski, IEEE Trans. Plasma Sci. **23**, 1006 (1995).
 [3] M. A. Sobolewski, J. G. Langan, and B. S. Felker, J. Vac. Sci. Technol. B **16**, 173 (1998).

- [4] H. R. Koenig and L. I. Maissel, IBM J. Res. Dev. **14**, 168 (1970).
 [5] C. M. Horwitz, J. Vac. Sci. Technol. A **1**, 60 (1983).
 [6] K. Kohler, J. W. Coburn, D. E. Horne, E. Kay, and J. H. Keller, J. Appl. Phys. **57**, 59 (1985).

- [7] A. M. Pointu, *Appl. Phys. Lett.* **48**, 762 (1986).
- [8] A. M. Pointu, *J. Appl. Phys.* **60**, 4113 (1986).
- [9] M. A. Lieberman, *J. Appl. Phys.* **65**, 4186 (1989).
- [10] M. A. Lieberman and S. E. Savas, *J. Vac. Sci. Technol. A* **8**, 1632 (1990).
- [11] P. A. Miller, L. A. Romero, and P. D. Pochan, *Phys. Rev. Lett.* **71**, 863 (1993).
- [12] J. Forster, *Appl. Phys. Lett.* **62**, 3429 (1993).
- [13] B. E. Thompson, K. D. Allen, A. D. Richards, and H. H. Sawin, *J. Appl. Phys.* **59**, 1890 (1986).
- [14] K. D. Allen and H. H. Sawin, *J. Electrochem. Soc.* **133**, 2326 (1986).
- [15] A. J. Van Roosmalen, *Appl. Phys. Lett.* **42**, 416 (1983).
- [16] B. Andries, G. Ravel, and L. Peccoud, *J. Vac. Sci. Technol. A* **7**, 2774 (1989).
- [17] T. Yamashita, S. Hasaki, I. Natori, H. Fukui, and T. Ohmi, *IEEE Trans. Semicond. Manuf.* **5**, 223 (1992).
- [18] M. Klick, W. Rehak, and M. Kammeyer, *Jpn. J. Appl. Phys., Part 1* **36**, 4625 (1997).
- [19] J. H. Keller, J. C. Forster, and M. S. Barnes, *J. Vac. Sci. Technol. A* **11**, 2487 (1993).
- [20] J. Asmussen, *J. Vac. Sci. Technol. A* **7**, 883 (1989).
- [21] J. M. Cook, D. E. Ibbotson, and D. L. Flamm, *J. Vac. Sci. Technol. B* **8**, 1 (1990).
- [22] R. W. Boswell and R. K. Porteous, *Appl. Phys. Lett.* **50**, 1130 (1987).
- [23] M. Surendra, C. R. Guarnieri, G. S. Selwyn, and M. Dalvie, *Appl. Phys. Lett.* **66**, 2415 (1995).
- [24] T. E. Nitschke and D. B. Graves, *IEEE Trans. Plasma Sci.* **23**, 717 (1995).
- [25] R. J. Hoekstra and M. J. Kushner, *J. Appl. Phys.* **79**, 2275 (1996).
- [26] M. J. Grapperhaus and M. J. Kushner, *J. Appl. Phys.* **81**, 569 (1997).
- [27] Y. Ra and C.-H. Chen, *J. Vac. Sci. Technol. A* **11**, 2911 (1993).
- [28] M. A. Sobolewski, *Appl. Phys. Lett.* **72**, 1146 (1998).
- [29] F. R. Myers and T. S. Cale, *J. Electrochem. Soc.* **139**, 3587 (1992).
- [30] M. Klick, *Phys. Rev. E* **47**, 591 (1993).
- [31] M. A. Lieberman, *IEEE Trans. Plasma Sci.* **16**, 638 (1988).
- [32] M. A. Lieberman, *IEEE Trans. Plasma Sci.* **17**, 338 (1989).
- [33] P. M. Vallinga, P. M. Meijer, and F. J. de Hoog, *J. Phys. D* **22**, 1650 (1989).
- [34] S. Biehler, *Appl. Phys. Lett.* **54**, 317 (1989).
- [35] V. A. Godyak and N. Sternberg, *Phys. Rev. A* **42**, 2299 (1990).
- [36] K. Bornig, *Appl. Phys. Lett.* **60**, 1553 (1992).
- [37] N. Sternberg and V. A. Godyak, *J. Comput. Phys.* **111**, 347 (1994).
- [38] M. Klick, *J. Appl. Phys.* **79**, 3445 (1996).
- [39] M. A. Sobolewski, *Phys. Rev. E* **56**, 1001 (1997).
- [40] J. H. Keller and W. B. Pennebaker, *IBM J. Res. Dev.* **23**, 3 (1979).
- [41] W. B. Pennebaker, *IBM J. Res. Dev.* **23**, 16 (1979).
- [42] A. Metzke, D. W. Ernie, and H. J. Oskam, *J. Appl. Phys.* **60**, 3081 (1986).
- [43] P. M. Vallinga and F. J. de Hoog, *J. Phys. D* **22**, 925 (1989).
- [44] P. A. Miller and M. E. Riley, *J. Appl. Phys.* **82**, 3689 (1997).
- [45] V. A. Godyak and R. B. Piejak, *J. Appl. Phys.* **68**, 3157 (1990).
- [46] V. A. Godyak, R. B. Piejak, and B. M. Alexandrovich, *J. Appl. Phys.* **69**, 3455 (1991).
- [47] M. A. Sobolewski, *Appl. Phys. Lett.* **70**, 1049 (1997).
- [48] P. J. Hargis, Jr., K. E. Greenberg, P. A. Miller, J. B. Gerardo, J. R. Torczynski, M. E. Riley, G. A. Hebner, J. R. Roberts, J. K. Olthoff, J. R. Whetstone, R. J. Van Brunt, M. A. Sobolewski, H. M. Anderson, M. P. Splichal, J. L. Mock, P. Bletzing, A. Garscadden, R. A. Gottscho, G. Selwyn, M. Dalvie, J. E. Heidenreich, J. W. Butterbaugh, M. L. Brake, M. L. Passow, J. Pender, A. Lujan, M. E. Elta, D. B. Graves, H. H. Sawin, M. J. Kushner, J. T. Verdeyen, R. Horwath, and T. R. Turner, *Rev. Sci. Instrum.* **65**, 140 (1994).
- [49] P. A. Miller, G. A. Hebner, K. E. Greenberg, P. D. Pochan, and B. P. Aragon, *J. Res. Natl. Inst. Stand. Technol.* **100**, 427 (1995).
- [50] A. Schwabedissen, E. C. Benck, and J. R. Roberts, *Phys. Rev. E* **55**, 3450 (1997).
- [51] The identification of commercial materials and their sources is made to foster understanding. In no case does this identification imply recommendation by the National Institute of Standards and Technology nor does it imply that the instrument is the best available.
- [52] M. A. Sobolewski and J. R. Whetstone, *Proc. SPIE* **1803**, 309 (1992).
- [53] M. A. Sobolewski, *J. Vac. Sci. Technol. A* **10**, 3550 (1992).
- [54] P. L. G. Ventzek, M. Grapperhaus, and M. J. Kushner, *J. Vac. Sci. Technol. B* **12**, 3118 (1994).
- [55] Y. Yamauchi and R. Shimizu, *Jpn. J. Appl. Phys., Part 2* **22**, L227 (1983).
- [56] M. A. Lewis, D. A. Glocker, and J. Jorne, *J. Vac. Sci. Technol. A* **7**, 1019 (1989).
- [57] C. D. Child, *Phys. Rev.* **32**, 492 (1911).
- [58] A. Schwabedissen (unpublished).
- [59] D. Martin and H. Oechsner, *Vacuum* **47**, 1017 (1996).
- [60] R. Clay, *Nonlinear Networks and Systems* (Wiley, New York, 1971).
- [61] L. J. Overzet and F. Y. Leong-Rousey, *Plasma Sources Sci. Technol.* **4**, 432 (1995).
- [62] M. A. Sobolewski, Y. Wang, and J. K. Olthoff (unpublished).